



OPEN

First principle simulation of coated hydroxychloroquine on Ag, Au and Pt nanoparticles

Razieh Morad^{1,2,4}, Mahmood Akbari^{1,2,4}, Parham Rezaee^{3,4}, Amin Koochaki^{3,4}, Malik Maaza^{1,2}✉ & Zahra Jamshidi³✉

From the first month of the COVID-19 pandemic, the potential antiviral properties of hydroxychloroquine (HCQ) and chloroquine (CQ) against SARS-CoV-2 suggested that these drugs could be the appropriate therapeutic candidates. However, their side effects directed clinical tests towards optimizing safe utilization strategies. The noble metal nanoparticles (NP) are promising materials with antiviral and antibacterial properties that can deliver the drug to the target agent, thereby reducing the side effects. In this work, we applied both the quantum mechanical and classical atomistic molecular dynamics approaches to demonstrate the adsorption properties of HCQ/CQ on Ag, Au, AgAu, and Pt nanoparticles. We found the adsorption energies of HCQ/CQ towards nanoparticles have the following trend: PtNP > AuNP > AuAgNP > AgNP. This shows that PtNP has the highest affinity in comparison to the other types of nanoparticles. The (non)perturbative effects of this drug on the plasmonic absorption spectra of AgNP and AuNP with the time-dependent density functional theory. The effect of size and composition of NPs on the coating with HCQ and CQ were obtained to propose the appropriate candidate for drug delivery. This kind of modeling could help experimental groups to find efficient and safe therapies.

Given that the process of developing new drugs to become appropriate clinical candidates is extensive, one of the most rapid and reliable treatments is drug repurposing—the examination of existing FDA approved drugs for new therapeutic purposes¹. Chloroquine (CQ) and hydroxychloroquine (HCQ) have been used for many years as pharmacotherapies for malaria and were recently proposed as a potential therapeutic option against COVID-19². The pre-clinical studies have shown the prophylactic and antiviral effects of CQ and HCQ against SARS-CoV-2 (or COVID-19)^{2–6}. The clinical safety profile for HCQ is better than that of CQ, thus allowing for long-term usage and higher daily dosage⁷. Some reports have mentioned that large scale (and prolonged) usage is potentially harmful and increases the risk of drug-induced torsades de pointes and may lead to cardiac death^{8–10}. Therefore, different treatment regimens try to focus on efficient strategies for in vivo usage of these drugs^{11,12}, especially the balance between the concentration of the drug in the blood and its severe potential toxicity, to ensure the safety of these therapeutic strategies^{7,13}. Despite conflicting evidence on the efficiency of HCQ for the treatment of COVID-19, the recent clinical studies have reported no potent evidence to support the benefit of HCQ as a treatment of COVID-19¹⁴.

Nanoparticles encapsulating drugs or attaching to therapeutics can be utilized as drug delivery systems to change drug biodistribution, decrease toxicity, modify drug release rate, and target affected tissues or cells^{15–18}. However, most nanoparticles are still in the clinical trial stage, with a few having been accepted for clinical use¹⁶. In this regard, noble metal nanoparticles are well-known as promising materials that can transport drugs to specific targets in the body and be engineered to develop new delivery systems¹⁹. Notably, silver, gold, and platinum nanoparticles reveal stability in the biological environment and survive in an intracellular environment^{20–22}. The stable nanoparticles with small size possess the advantage of easily interacting with biomolecules both on the surface and inside cells, thereby playing a significant role in biomedical applications such as drug vehicles in diagnosing and treating diseases.

¹UNESCO-UNISA Africa Chair in Nanoscience and Nanotechnology (U2ACN2), College of Graduate Studies, University of South Africa (UNISA), Pretoria, South Africa. ²Material Research Division, Nanoscience African Network (NANOAFNET), iThemba LABS-National Research Foundation, Somerset West 7129, South Africa. ³Chemistry Department, Sharif University of Technology, 11155-9516 Tehran, Iran. ⁴These authors contributed equally: Razieh Morad, Mahmood Akbari, Parham Rezaee and Amin Koochaki. ✉email: maaza@tlabs.ac.za; njamshidi@sharif.edu

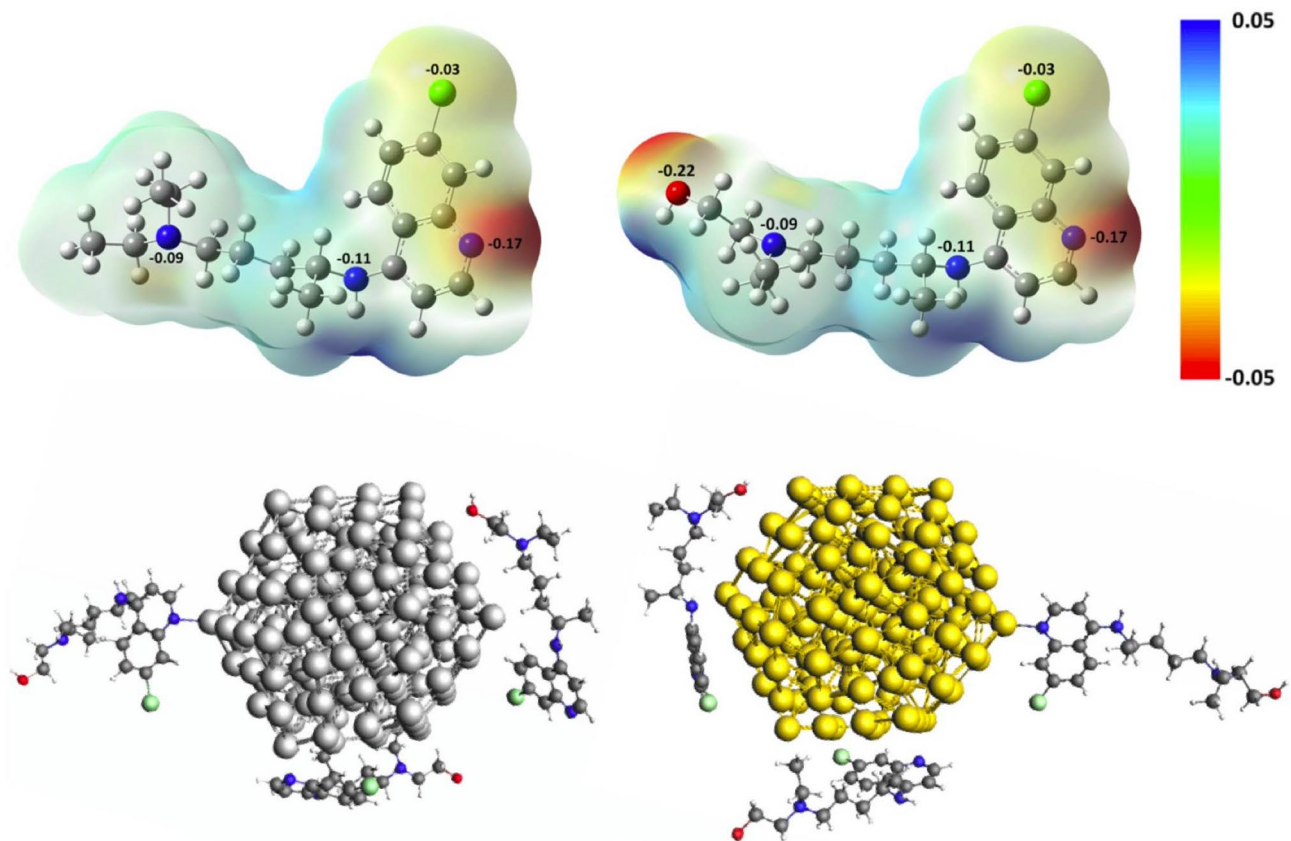


Figure 1. Charge distribution of HCQ and CQ molecules and their electrostatic potential map. Stable geometry of Ag_{147} and Au_{147} complexed with HCQ molecules (at BPE-D3/TZP level of theory).

Noble metals, especially silver, has a long history of usage as antibacterial materials^{23–26}, and current studies have utilized the antiviral and immunomodulatory properties of silver nanoparticles (AgNPs)^{27,28}. Recently, Garofalo et al.²⁹ demonstrated the *in vivo* antiviral activity of AgNPs during respiratory syncytial virus (RSV) infection. On the other hand, the biocompatibility and easy synthesis process of gold nanoparticles (AuNPs) as another noble metal, makes them appropriate candidates in the drug delivery system^{30,31}, especially in cancer therapies^{32,33}. Although Ag, Au, and Pt compounds are well-known for being safe for humans, the toxicity of nanoparticles should be carefully considered in nanomedicine. In this regard, previous studies have indicated that PtNP is less toxic compared to AgNPs³⁴. Furthermore, different green synthesized processes have been proposed to potentially decrease the toxicity issues of nanoparticles and their side-effects in medications^{35–38}. However, it is necessary to investigate their toxicity in more detail for their particular usage.

Current work is done under extended lockdown across the world, with no possibility of accessing experimental laboratories. In this situation, the work is just beginning for computational chemists and biophysicists to model the different approaches and propose efficient therapies to the experimentalists. Computational studies of molecular interactions of drugs can be used to develop the next-generation of drug inventions such as target-based drug discovery and delivery.

This paper has carried out the first principle density functional calculations to determine the affinity of HCQ/CQ molecules towards noble nanoparticles and confirm their weak interaction by theoretical UV–Vis absorption spectra. The slab model using plane wave DFT was used to demonstrate the trend in the affinity of the drug molecules towards the noble metal nanoparticles. The complementary calculations were done based on molecular dynamics simulations by changing the size and composition of metal nanoparticles and the number of coated HCQ molecules. Our computational findings on the interaction of noble nanoparticles with drugs suggest these materials as potential vehicles for efficient HCQ/CQ usage to decrease their side effects.

Computational details

For HCQ and CQ molecules, the geometry optimization and frequency calculation were performed with PBE generalized gradient (GGA) exchange–correlation (xc-) density functional³⁹ with the inclusion of the Grimme dispersion correction scheme (D3)^{40–42} applying Becke–Johnson damping and a triple- ζ polarized (TZP) Slater type basis set (PBE-D3/TZP). The Conductor like Screening Model (COSMO)⁴³ was considered to model the effect of water solvent. For the optimized structure, the Hirshfeld point charges⁴⁴ and electrostatic potential map were obtained both with and without the solvent (in Fig. 1 and Supplementary Fig. S1). The experimental interatomic metal–metal distance was employed to create starting structures for further optimization with the LDA (local density approximation) xc-functional⁴⁵ and the scalar relativistic ZORA formalism^{46,47}. The

interactions of HCQ with icosahedral silver and gold clusters with 147 atoms were investigated at the PBE-D3/TZP level of the theory under the influence of the relativistic effect (ZORA). To determine the effect of HCQ drug on the electronic structures and the plasmonic absorption spectra of noble metal particles, the recently developed time-dependent density functional approach, TD-DFT + TB method^{48,49} which combines a full DFT ground state with tight-binding approximations, was applied. The excited states calculations were performed at optimized geometries using the asymptotically corrected LB94 xc-functional⁵⁰, and the absorption spectra were obtained in the range of 0.0–6.0 eV. All these calculations were performed with the Amsterdam Density Functional (ADF2019.1) program⁵¹.

A periodic slab model has been considered to study the adsorption of HCQ molecules on the Ag(111), Au(111), and Pt(111) surfaces using the Quantum ESPRESSO package⁵² with PBE-D3^{39,40} functional. The cut-off energy of 80 Rydberg (~ 1088 eV) was employed for the plane-wave basis set, and the electron–ion interactions were represented through the ultrasoft pseudopotential, including the scalar relativistic effects. The slab is made of four layers of Ag/Au/Pt with 36 atoms per layer. A large vacuum in the z-direction (perpendicular to the slab) was applied, and the large size of the box made it possible that just the Γ -point of the reciprocal lattice was considered. During the calculations, the first two layers were kept fixed at the bulk positions while the atoms in the top layers and molecule were allowed to relax.

The molecular dynamics (MD) simulations for interactions of HCQ and CQ with noble metal nanoparticles (NPs), Ag₁₄₇, Au₁₄₇, Au₉₂Ag₅₅, and Pt₁₄₇ were performed in a cubic box with sides of $60 \times 60 \times 60$ Å (structures are available in Supplementary Table S1–S6). The nanoparticles were fixed at the center of the box and were surrounded by water molecules in a random arrangement and either HCQ or CQ drugs. The time step in the simulation was 2.0 fs, and the length of time is 20 ns, under the isothermal-isobaric NPT (constant particle number, pressure, and temperature) condition at 300 K and 1 atm (controlled with Nose–Hoover algorithm). The OPLS-AA⁵³ and TIP3P⁵⁴ force fields were used to describe the interactions of drugs and water molecules, respectively. Moreover, the Lennard–Jones parameters for nanoparticles are listed in Supplementary Table S7. The electrostatic interactions were simulated with the Particle–Particle–Mesh (PPPM)⁵⁵ solver (with accuracy 1×10^{-5}). The non-bonded dispersion interactions were computed with Lennard–Jones (LJ) 12–6 potential with the cut-off distance of 12 Å.

To study the effects of nanoparticle size, four different sizes of AgNPs with 147, 561, 1415, 2869 atoms (with diameter 1.6, 2.6, 3.6, and 4.6 nm, respectively) were placed at the simulation box with fixed (i.e., 12) and a varying number of HCQ molecules (i.e., 12, 32, 64, 105) that increased proportionally with the number of silver atoms on the surface. The simulation box was filled with 6000 water molecules. All simulations were performed using the Gromos53a6⁵⁶ and SPC⁵⁴ force fields. The energy was minimized by using the steepest descent minimization algorithm⁵⁷. Equilibration of each system was done in three steps. First, an NVT ensemble coupled to the V-rescale thermal bath at 300 K was applied to the system over 100 ps. Then, an NPT ensemble coupled to the Berendsen pressure bath at 1 atm over 200 ps was applied to the system. Finally, the system was subjected to a 50 ns molecular dynamics (MD) simulation under constant conditions of 1 atm and 300 K with a time step of 1 fs. The LINCS algorithm⁵⁸ was used to constraint the bond lengths, and the long-range electrostatics were applied using the particle mesh Ewald (PME)⁵⁹. The LAMMPS⁶⁰ and GROMACS packages^{61,62} were used for molecular dynamics simulations, and the VMD package⁶³ was used for the visualization.

Results and discussion

Interaction of HCQ with AgNP and AuNP and its influence on absorption spectra. The charge distribution of HCQ and CQ molecules and their electrostatic potential map in Fig. 1 displays the active sites of these molecules for interaction with noble metal NPs. The initial structure of complexes was generated by placing the small silver cluster near the electron-rich sites (e.g., N-, O- and Cl- groups). These sites can donate the electron density via their lone pairs to 4d and 5s orbitals of the silver atom^{64,65}. The nitrogen of the pyridine ring in CQ and HCQ and the oxygen of the hydroxyl group in HCQ have the highest affinity for interaction with noble metal clusters. Moreover, the optimized structure of HCQ/CQ on Ag(111), Au(111), and Pt(111) layers exhibited the highest affinity of drug molecules toward the platinum surface, and their charge density difference confirmed the transfer of charge and accumulation on the metal surface (see Fig. 2, Supplementary Fig. S2, and Supplementary Table S8).

In addition, Fig. 1 shows the stable geometry of icosahedral Ag₁₄₇ and Au₁₄₇ nanoparticles which are complexed with HCQ molecules (at PBE-D3/TZP level of theory). Here, the non-covalent charge-transfer interactions with partially negative charge groups of the molecule play an essential role in determining the ability of nanoparticles to bond with HCQ or CQ. The binding energy of HCQ with AgNP (at PBE-D3/TZP level of theory) is about $\Delta E_b = -21.06$ kcal mol⁻¹ (per HCQ molecule), while the interaction energy with AuNP is about $\Delta E_b = -29.39$ kcal mol⁻¹ more favorable than silver. The higher electron affinity of gold ($EA_{Au} = 2.31$ eV) compared to silver ($EA_{Ag} = 1.30$ eV)⁶⁶ gives rise to increasing the interaction energy of gold atoms towards the lone-pair of HCQ. This is also confirmed by the density difference map and accumulation of negative charge on the Au(111) surface. In this regard, the adsorption energy of HCQ towards Pt(111) is about 60% more than the Au(111) surface (see Fig. 2, Supplementary Fig. S2, and Supplementary Table S8).

The absorption UV–Vis spectrum of bare nanoparticles and its variation under the effect of coated compounds provides further crucial evidence that can be compared with the experimental results. The spectrum can accurately estimate the effect of adsorbent molecules on the variation of electronic structures of metal NPs. Silver and gold nanoparticles are well-known for their high-intensity plasmonic absorption spectra in the UV–Vis range that can be varied by coating with the drugs. Here, the TD-DFT + TB calculations for the optimized AgNP–HCQ and AuNP–HCQ complexes compared to bare nanoparticles were obtained. TD-DFT + TB, as an accurate and efficient approach, obtained the ground-state orbitals with DFT and the excited-state properties with the

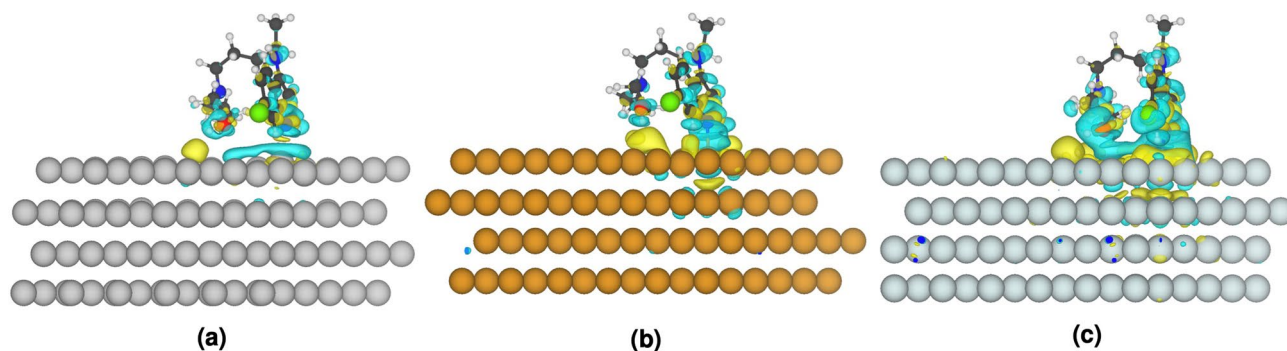


Figure 2. The charge density difference of adsorbed of HCQ molecules on a periodic slab model of Ag(111), Au(111), and Pt(111). The isovalue for the charge transfer plot, is fixed at $0.001e/a.u.^3$. Yellow and blue colors indicate positive and negative level corresponds to gain and loss of electron density.

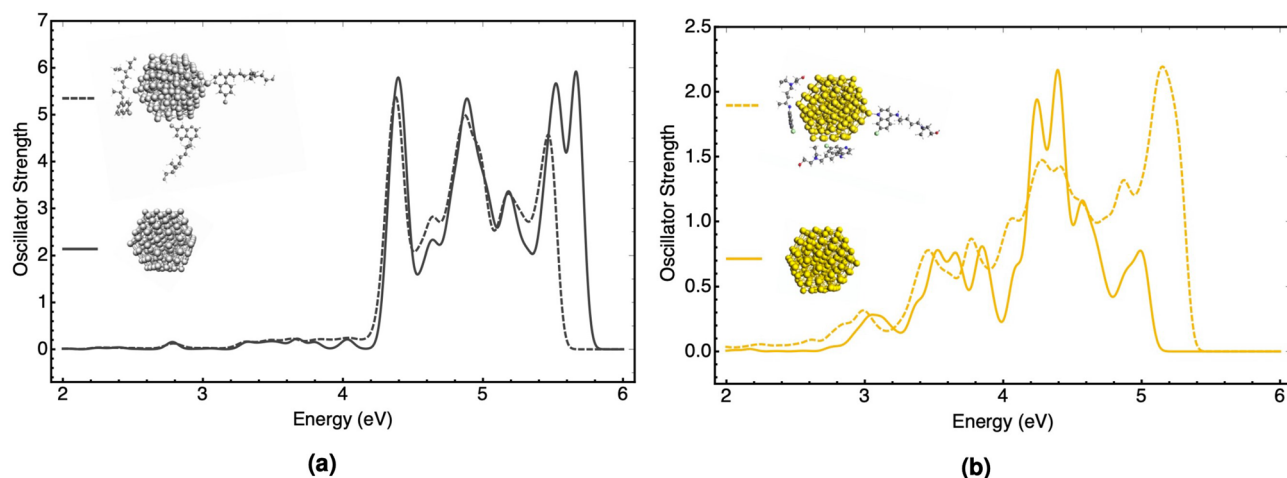


Figure 3. Comparison of the plasmonic absorption spectra of bare (solid line) and complexed (dash line) for (a) AgNP-HCQ and (b) AuNP-HCQ at the TD-DFT + TB level of theory. Spectra have been broadened with a $\sigma = 0.1$ eV Gaussian.

tight-binding method. As shown in Fig. 3, for the AgNP-HCQ complex, the plasmonic spectrum compared to bare AgNP did not change clearly, and just the intensity of peaks around 5.5 eV damped slightly. On the other hand, for the AuNP-HCQ complex after the adsorption of HCQ, the plasmonic peak of gold in the range of 4.0–4.5 eV exhibited a distinct variation in energy and intensity. The shift of the high-intensity peak to blue established the more perturbative effect of HCQ adsorption on the electronic structure and plasmonic spectrum of AuNP in comparison to AgNP.

AgNP, AuNP, AgAuNP, and PtNP coated with HCQ(CQ). In this part, the effect of changing the type of nanoparticles and increasing the number of HCQ molecules on the coating properties of nanoparticles are discussed based on molecular dynamics calculations and the trend of the radial distribution function (RDF). RDF depicts how the density of one molecule changes as a function of the distance from another reference molecule. Besides, RDF can be used to represent distance-dependent relative probability for observing a given site (or atom) relative to some central site (or atom). This analysis provides the microstructure information about the arrangement of HCQ/CQ molecules and their affinity for interactions with nanoparticles^{67–69}.

Figure 4 displays the RDF, $g(r)$, for the active sites of HCQ/CQ molecules with different types of (147-atomic icosahedral) nanoparticles such as AgNP, AuNP, AgAuNP, and PtNP. As can be found in Fig. 4, the nitrogen of the pyridine ring has the highest affinity in comparison to other types of nitrogen, which is in agreement with the DFT calculation in the previous section. However, it can be seen in Fig. 4 that the peak of chlorine increases in the same way as nitrogen, which can be related to its vicinity to the nitrogen atom of the pyridine ring and not the affinity of the Cl-group. The minimum DFT structure (in the previous section) and the lower negative charge of Cl ($-0.03|e|$) in comparison to N ($-0.17|e|$) further strengthen this claim. In addition, the coating of Ag₁₄₇ with more HCQ molecules was simulated (in Supplementary Fig. S6a), which confirmed higher $g(r)$ for N-group with respect to Cl-group. The probability distribution map of atoms near the nanoparticles (see Supplementary Fig. S3–S4 in supporting information) confirms the RDF results.

Furthermore, the O-atom of the hydroxyl group is another active site of HCQ for interaction. However, for gold, silver, and alloy nanoparticles, the $g(r)$ values for O-group is lower than N-group, and for PtNP, it is

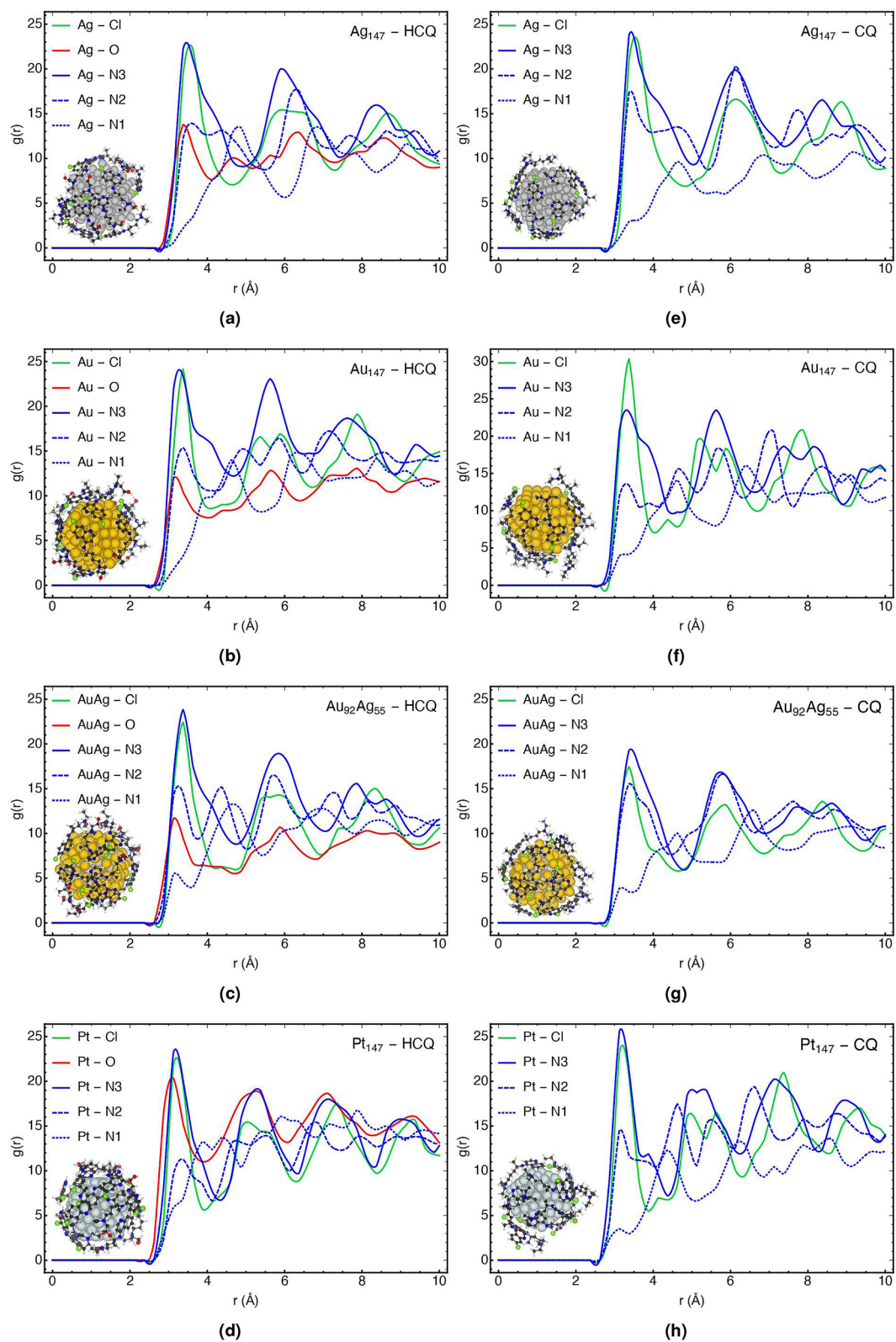


Figure 4. RDF plots for the active sites of H₂C/CQ with different types of (147-atomic icosahedral) nanoparticles such as AgNP, AuNP, AgAuNP, and PtNP.

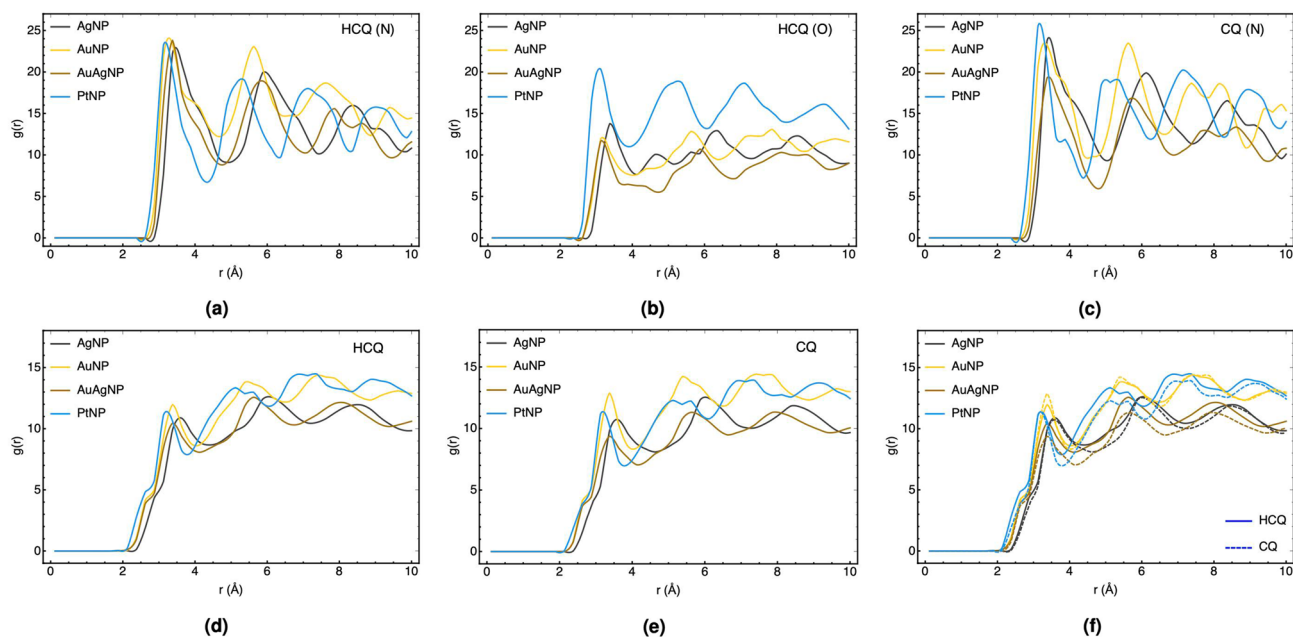


Figure 5. Comparison of the total and atom type RDF plots for HCQ/CQ molecules with AgNP, AuNP, AuAgNP, and PtNP.

slightly more than N-group. For PtNP–HCQ in Fig. 4d, the approximately similar RDF peaks around 3.0 Å for both O-group and N-group can be related to the high affinity of the PtNP to interact with both sides of HCQ. For gold and silver noble metals, the higher attraction of N-group (verse O-group) was established by Antusek et al. based on ab-initio calculation⁷⁰.

Figure 5 compares the total and atom type RDFs of HCQ/CQ molecules with respect to the variation of nanoparticles to propose the possible candidates for adsorption. Figure 5a–c compares the RDF of N- and O-atom of HCQ and N-atom of CQ with respect to the type of nanoparticles. For N-group, the affinity of different types of nanoparticles is nearly similar to each other, although PtNP has numerous robust peaks in the range of < 10 Å. On the other hand, the sharp and intense $g(r)$ peak for O-group with PtNP, which appears at a shorter distance, demonstrates the best adsorption properties on PtNP and explains the stronger affinity of PtNP to HCQ compared to CQ. Accordingly, we can conclude that HCQ preferred to adsorb on AuNP, AgNP, and alloy from one side and coated on PtNP by N- and O-group.

Finally, Fig. 5d,e show the total RDF plots of HCQ and CQ molecules with respect to the type of nanoparticles and demonstrated that the overall coating trend is as follows: PtNP > AuNP > AuAgNP > AgNP. Additionally, comparing the total RDF of NPs with HCQ and CQ (Fig. 5f) indicates that PtNP has a higher $g(r)$ and more affinity towards HCQ than CQ, which is in agreement with our DFT results presented in Supplementary Table S8.

Coated HCQ on the different size of Ag_n ($n = 147, 561, 1415, \text{ and } 2869$). In this part, the effect of the size on the adsorption properties of AgNPs is investigated. The calculated diameters of Ag_{147} , Ag_{561} , Ag_{1415} , and Ag_{2869} nanoparticles are 1.6, 2.6, 3.6, and 4.6 nm, respectively, while their thickness after coating with HCQ increases about 1 nm. The AgNPs are coated with the fixed number of HCQ (12 molecules) interacting with the twelve active sites in their corners. In another attempt, the AgNPs with different sizes are coated with 12, 32, 64, and 105 molecules, proportional to the numbers of their surface atoms.

As can be found in Supplementary Fig. S5, coating nanoparticles with HCQ molecules exhibit significant fluctuations at the beginning of the simulations, indicating the free movement of HCQ molecules near the nanoparticles due to the spatial setting of the medicines in the active site. However, after ~ 5 ns, the fluctuations disappear, maintaining a continuous equilibrium to the end of the simulation time. These results suggest the reliable stabilities of the dynamic equilibriums for the complexes and their trajectories could be useful in collecting snapshots for further analyses (see Supplementary Fig. S5).

In Fig. 6 (and Supplementary Fig. S6 and S7), the RDF plots for the fixed and varying numbers of HCQ with respect to the size of AgNPs and the type of anchoring atoms are displayed. The comparison of the RDF plots for the N-group as an active-site (Fig. 6b), in addition to all atoms (Fig. 6a), exhibits a decreasing trend in the adsorption properties by going from small to larger AgNPs. The same trend was reproduced in Fig. 6c,d, in which the portion of HCQs increases with respect to the number of atoms on the surface. Generally, the overall coating properties decrease as the size of nanoparticles increases from 1.6 to 4.6 nm (see Supplementary Fig. S8). It has been established that the affinity of noble metal clusters is lowered by increasing their size. Moreover, in agreement with the previous section, the N-group has a higher affinity for interaction with different size of AgNPs with respect to the O-group (see Supplementary Fig. S6 and S7). Finally, Supplementary Fig. S8 shows the comparison of RDF for HCQ and CQ coated on Ag_{2869} and reveals the appropriate adsorption affinity of HCQ versus CQ.

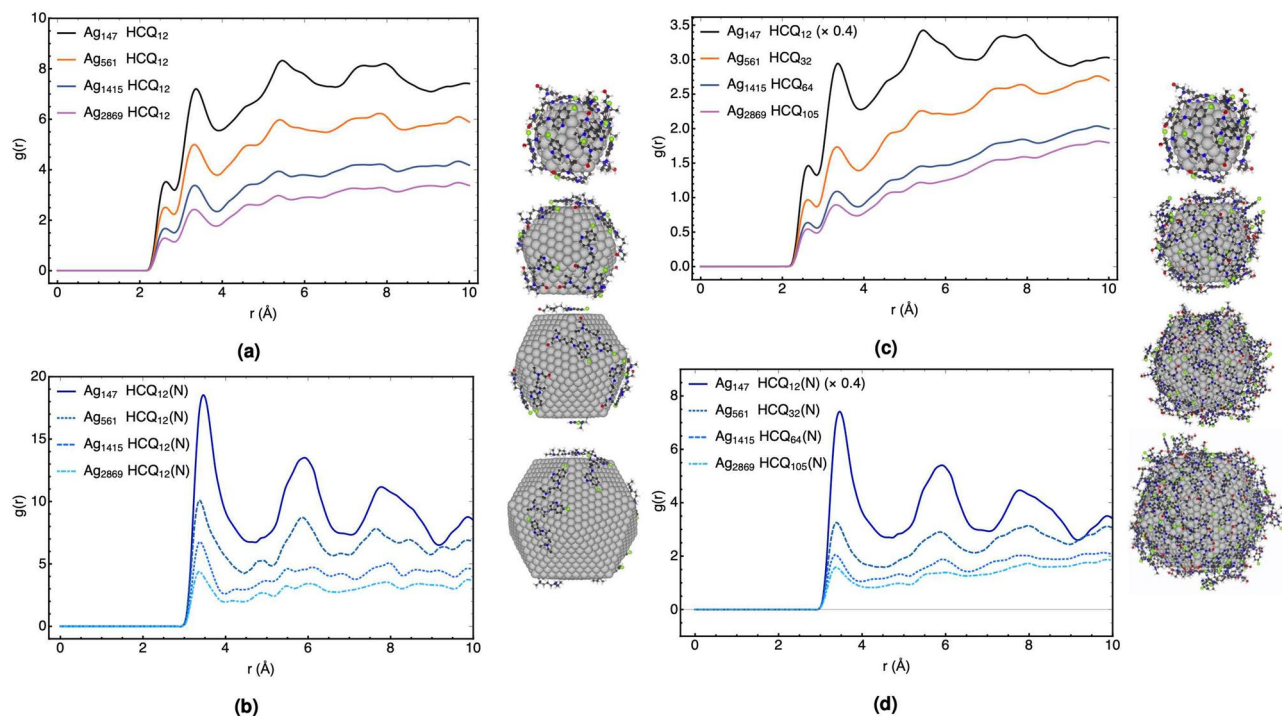


Figure 6. RDF of HCQ with different size of AgNPs. **(a,b)** AgNPs are coated with the same number of HCQ molecules. **(c,d)** AgNPs are coated with the different number of HCQ molecules.

Conclusion

In summary, the adsorption and the coating properties of noble metal nanoparticles with HCQ/CQ molecules have been studied as a potentially efficient strategy for in vivo usage of these drugs. The weak charge-transfer interaction with partially negative charge groups of drugs was investigated, and it was established by changing the type of nanoparticle elements that the affinity towards N and O groups increases as follows: AgNP < AuAgNP < AuNP < PtNP. Following the investigation of the effect of size on the coating properties, it was found that the overall affinity decreases by increasing the size from 1.6 nm (for Ag₁₄₇) to 2.6 nm (for Ag₅₆₁). For Ag₅₆₁, Ag₁₄₁₅, and Ag₂₈₆₉ with diameters 2.6 to 4.6 nm, a nearly similar decrease in affinity was obtained. Finally, based on the quantum mechanics and molecular dynamics simulation, we can suggest these noble nanoparticles (with low toxicity and antiviral activity) as appropriate vehicles for efficient HCQ/CQ usage with decreased side effects of the drugs.

Data availability

No datasets were generated or analyzed during the current study.

Received: 4 June 2020; Accepted: 6 January 2021

Published online: 22 January 2021

References

- Shah, A., Kashyap, R., Tosh, P., Sampathkumar, P. & O'Horo, J. C. Guide to understanding the 2019 novel coronavirus. *Mayo Clin. Proc.* **95**, 646–652 (2020).
- Liu, J. *et al.* Hydroxychloroquine, a less toxic derivative of chloroquine, is effective in inhibiting SARS-CoV-2 infection in vitro. *Cell Discov.* **6**, 16 (2020).
- Wang, M. *et al.* Remdesivir and chloroquine effectively inhibit the recently emerged novel coronavirus (2019-nCoV) in vitro. *Cell Res.* **30**, 269–271 (2020).
- Yao, X. *et al.* In vitro antiviral activity and projection of optimized dosing design of hydroxychloroquine for the treatment of severe acute respiratory syndrome coronavirus 2 (SARS-CoV-2). *Clin. Infect. Dis.* **71**, 732–739 (2020).
- Gautret, P. *et al.* Hydroxychloroquine and azithromycin as a treatment of COVID-19: results of an open-label non-randomized clinical trial. *Int. J. Antimicrob. Agents* **56**, 105949 (2020).
- Geleris, J. *et al.* Observational study of hydroxychloroquine in hospitalized patients with Covid-19. *N. Engl. J. Med.* **382**, 2411–2418 (2020).
- Giudicessi, J. R., Noseworthy, P. A., Friedman, P. A. & Ackerman, M. J. Urgent guidance for navigating and circumventing the QTc-prolonging and torsadogenic potential of possible pharmacotherapies for coronavirus disease 19 (COVID-19). *Mayo Clin. Proc.* **95**, 1213–1221 (2020).
- Lecuit, M. Chloroquine and COVID-19, where do we stand?. *Med. Maladies Infect.* **50**, 229–230 (2020).
- Karatzas, E., Ismailos, G., Marangos, M. & Karalis, V. Optimization of hydroxychloroquine dosing scheme based on COVID-19 patients' characteristics: a review of the literature and simulations. *Xenobiotica* <https://doi.org/10.1080/00498254.2020.1824301> (2020).
- White, N. J. *et al.* COVID-19 prevention and treatment: A critical analysis of chloroquine and hydroxychloroquine clinical pharmacology. *PLoS Med* **17**, e1003252 (2020).

11. Colson, P., Rolain, J.-M., Lagier, J.-C., Brouqui, P. & Raoult, D. Chloroquine and hydroxychloroquine as available weapons to fight COVID-19. *Int. J. Antimicrob. Agents* **55**, 105932 (2020).
12. Pastick, K. A. *et al.* Review: Hydroxychloroquine and chloroquine for treatment of SARS-CoV-2 (COVID-19). *Open Forum Infect. Dis.* **7**, 130 (2020).
13. Holshue, M. L. *et al.* First case of 2019 novel coronavirus in the United States. *N. Engl. J. Med.* **382**, 929–936 (2020).
14. Torjsten, I. Covid-19: Hydroxychloroquine does not benefit hospitalised patients, UK trial finds. *BMJ* **369**, m2263 (2020).
15. Pushpalatha, R., Selvamuthukumar, S. & Kilimozhi, D. Nanocarrier mediated combination drug delivery for chemotherapy—A review. *J. Drug Deliv. Sci. Technol* **39**, 362–371 (2017).
16. Patra, J. K. *et al.* Nano based drug delivery systems: Recent developments and future prospects. *J. Nanobiotechnol* **16**, 71 (2018).
17. Rai, M., Ingle, A. P., Birla, S., Yadav, A. & Santos, C. A. D. Strategic role of selected noble metal nanoparticles in medicine. *Crit. Rev. Microbiol.* **42**, 696–719 (2015).
18. Jeyaraj, M., Gurunathan, S., Qasim, M., Kang, M.-H. & Kim, J.-H. A comprehensive review on the synthesis, characterization, and biomedical application of platinum nanoparticles. *Nanomaterials* **9**, 1719 (2019).
19. Ravindra, S. *et al.* Development and characterization of curcumin loaded silver nanoparticle hydrogels for antibacterial and drug delivery applications. *J. Inorg. Organomet. Polym. Mater.* **22**, 1254–1262 (2012).
20. Burdusel, A.-C. *et al.* Biomedical applications of silver nanoparticles: An up-to-date overview. *Nanomaterials* **8**, 681 (2018).
21. Pedone, D., Moglianetti, M., De Luca, E., Bardi, G. & Pompa, P. P. Platinum nanoparticles in nanobiomedicine. *Chem. Soc. Rev.* **46**, 4951–4975 (2017).
22. Pena Gonzalez, C. E. *et al.* Dendronized anionic gold nanoparticles: Synthesis, characterization, and antiviral activity. *Chem. Eur. J.* **22**, 2987–2999 (2016).
23. Geraldo, D. A. *et al.* Green synthesis of polysaccharides-based gold and silver nanoparticles and their promissory biological activity. *Biointerface Res. Appl. Chem.* **6**, 1263–1271 (2016).
24. Chowdhury, N. R., MacGregor-Ramiassa, M., Zilm, P., Majewski, P. & Vasilev, K. 'Chocolate' silver nanoparticles: Synthesis, antibacterial activity and cytotoxicity. *J. Colloid Interface Sci.* **482**, 151–158 (2016).
25. Tavaf, Z., Tabatabaei, M., Khalafi-Nezhad, A. & Panahi, F. Evaluation of antibacterial, antibiofilm and antioxidant activities of synthesized silver nanoparticles (AgNPs) and casein peptide fragments against *Streptococcus mutans*. *Eur. J. Integr. Med.* **12**, 163–171 (2017).
26. Henke, P. *et al.* Antibacterial, antiviral, and oxygen-sensing nanoparticles prepared from electrospun materials. *ACS Appl. Mater. Interfaces.* **8**, 25127–25136 (2016).
27. Galdiero, S. *et al.* Silver nanoparticles as potential antiviral agents. *Molecules* **16**, 8894–8918 (2011).
28. Villeret, B. *et al.* Silver nanoparticles impair retinoic acid-inducible gene I-mediated mitochondrial antiviral immunity by blocking the autophagic flux in lung epithelial cells. *ACS Nano* **12**, 1188–1202 (2018).
29. Morris, D. *et al.* Antiviral and immunomodulatory activity of silver nanoparticles in experimental RSV infection. *Viruses* **11**, 732 (2019).
30. Wang, L. S., Chuang, M. C. & Ho, J. A. A. Nanotheranostics—A review of recent publications. *Int. J. Nanomed.* **7**, 4679–4695 (2012).
31. Falagan-Lotsch, P., Grzincic, E. M. & Murphy, C. J. New advances in nanotechnology-based diagnosis and therapeutics for breast cancer: An assessment of active-targeting inorganic nanoplateforms. *Bioconjugate Chem.* **28**, 135–152 (2017).
32. Her, S., Jaffray, D. A. & Allen, C. Gold nanoparticles for applications in cancer radiotherapy: Mechanisms and recent advancements. *Adv. Drug Deliv. Rev.* **109**, 84–101 (2017).
33. Dreaden, E. C. *et al.* Antiandrogen gold nanoparticles dual-target and overcome treatment resistance in hormone-insensitive prostate cancer cells. *Bioconjugate Chem.* **23**, 1507–1512 (2012).
34. Asharani, P. V., Lianwu, Y., Gong, Z. & Valiyaveetil, S. Comparison of the toxicity of silver, gold and platinum nanoparticles in developing zebrafish embryos. *Nanotoxicology* **5**, 43–54 (2011).
35. Lam, P. L., Wong, W. Y., Bian, Z., Chui, C. H. & Gambari, R. Recent advances in green nanoparticulate systems for drug delivery: Efficient delivery and safety concern. *Nanomedicine* **12**, 357–385 (2017).
36. Shakeel, A., Mudasar, A., Babu Lal, S. & Saiqa, I. A review on plants extract mediated synthesis of silver nanoparticles for antimicrobial applications: A green expertise. *J. Adv. Res.* **7**, 17–28 (2016).
37. Prabhu, S. & Poulouse, E. K. Silver nanoparticles: mechanism of antimicrobial action, synthesis, medical applications, and toxicity effects. *Int. Nano Lett.* **2**, 32 (2012).
38. Jahangirian, H., Lemraski, E. G., Webster, T. J., Rafiee-Moghaddam, R. & Abdollahi, Y. A review of drug delivery systems based on nanotechnology and green chemistry: Green nanomedicine. *Int. J. Nanomed.* **12**, 2957 (2017).
39. Perdew, J. P., Burke, K. & Ernzerhof, M. Generalized gradient approximation made simple. *Phys. Rev. Lett.* **77**, 3865–3868 (1996).
40. Grimme, S., Ehrlich, S. & Goerigk, L. Effect of the damping function in dispersion corrected density functional theory. *J. Comput. Chem.* **327**, 1456–1465 (2011).
41. Fonseca Guerra, C., Snijders, J. G., te Velde, G. & Baerends, E. J. Towards an order-N DFT method. *Theoret. Chem. Acc.* **99**, 391 (1998).
42. Handy, N. C. & Cohen, A. J. Left-right correlation energy. *Mol. Phys.* **99**, 403–412 (2001).
43. Klamt, A. & Schuurmann, G. COSMO: A new approach to dielectric screening in solvents with explicit expressions for the screening energy and its gradient. *J. Chem. Soc. Perkin Trans.* **25**, 799–805 (1993).
44. Schrier, J. Carbon dioxide separation with a two-dimensional polymer membrane. *ACS Appl. Mater. Interfaces* **4**, 3745–3752 (2012).
45. Vosko, S. H., Wilk, L. & Nusair, M. Accurate spin-dependent electron liquid correlation energies for local spin density calculations: A critical analysis. *Can. J. Phys.* **58**, 1200–1211 (1980).
46. Pierloot, K. & Vancoillie, S. Relative energy of the high-(5T_{2g}) and low-(1A_{1g}) spin states of the ferrous complexes [Fe(L)(NHS₄): CASPT2 versus density functional theory. *J. Chem. Phys.* **128**, 034104 (2008).
47. Van Lenthe, E., Snijders, J. G. & Baerends, E. J. The zero-order regular approximation for relativistic effects: The effect of spin-orbit coupling in closed shell molecules. *J. Chem. Phys.* **105**, 6505–6516 (1996).
48. Rüger, R., van Lenthe, E., Heine, T. & Visscher, L. Tight-binding approximations to time-dependent density functional theory—A fast approach for the calculation of electronically excited states. *J. Chem. Phys.* **144**, 184103 (2016).
49. Asadi-Aghbolaghi, N., Ruger, R., Jamshidi, Z. & Visscher, L. TD-DFT+TB: An efficient and fast approach for quantum plasmonic excitations. *J. Chem. Phys.* **124**, 7946–7955 (2020).
50. van Leeuwen, R. & Baerends, E. J. Exchange-correlation potential with correct asymptotic behavior. *Phys. Rev. A* **49**, 2421–2431 (1994).
51. te Velde, G. *et al.* Chemistry with ADF. *J. Comput. Chem.* **22**, 931–967 (2001).
52. Scandolo, S. *et al.* First-principles codes for computational crystallography in the quantum-ESPRESSO package. *Z. Kristallogr. Cryst. Mater.* **220**, 574–579 (2005).
53. Jorgensen, W. L. & Tirado-Rives, J. The OPLS [optimized potentials for liquid simulations] potential functions for proteins, energy minimizations for crystals of cyclic peptides and crambin. *J. Am. Chem. Soc.* **110**, 1657–1666 (1998).
54. Jorgensen, W. L., Chandrasekhar, J., Madura, J. D., Impey, R. W. & Klein, M. L. Comparison of simple potential functions for simulating liquid water. *J. Chem. Phys.* **79**, 926–935 (1983).
55. Hockney, R. W., Eastwood, J. W. *Computer Simulation Using Particles* (special student ed.) (A. Hilger, Bristol, 1988).

56. Kyrychenko, A., Pasko, D. A. & Kalugin, O. N. Poly(vinyl alcohol) as a water protecting agent for silver nanoparticles: The role of polymer size and structure. *Phys. Chem. Chem. Phys.* **19**, 8742–8756 (2017).
57. Phanchai, W., Srikulwong, U., Chompoosor, A., Sakonsinsiri, C. & Puangmali, T. Insight into the molecular mechanisms of AuNP-based aptasensor for colorimetric detection: A molecular dynamics approach. *Langmuir* **34**, 6161–6169 (2018).
58. Hess, B., Bekker, H., Berendsen, H. J. & Fraaije, J. G. LINCS: A linear constraint solver for molecular simulations. *J. Comput. Chem.* **18**, 1463–1472 (1997).
59. Plimpton, S. Fast parallel algorithms for short-range molecular dynamics. *J. Comput. Phys.* **117**, 1–19 (1995).
60. Plimpton, S., Pollock, R., Stevens, M. Particle-mesh Ewald and rRESPA for parallel molecular dynamics simulations. in *Proceedings of the Eighth SIAM Conference on Parallel Processing for Scientific Computing* (1997).
61. Abraham, M. J. *et al.* GROMACS: High performance molecular simulations through multilevel parallelism from laptops to supercomputers. *SoftwareX* **1–2**, 19–25 (2015).
62. Van Der Spoel, D. *et al.* GROMACS: Fast, flexible, and free. *J. Comput. Chem.* **26**, 1701–1718 (2005).
63. Humphrey, W., Dalke, A. & Schulten, K. VMD: Visual molecular dynamics. *J. Mol. Graph.* **14**, 33–38 (1996).
64. Pakiari, A. H. & Jamshidi, Z. Interaction of amino acids with gold and silver clusters. *J. Phys. Chem. A* **111**, 4391–4396 (2007).
65. Aliakbar Tehrani, Z., Jamshidi, Z., Jebeli Javan, M. & Fattahi, A. Interactions of glutathione tripeptide with gold cluster: Influence of intramolecular hydrogen bond on complexation behavior. *J. Phys. Chem. A* **116**, 4338–4347 (2012).
66. Granatier, J., Urban, M. & Sadlej, A. J. Van der Waals complexes of Cu, Ag, and Au with hydrogen sulfide: The bonding character. *J. Phys. Chem. A* **111**, 13238–13244 (2007).
67. Brehm, M. & Kirchner, B. TRAVIS—A free analyzer and visualizer for Monte Carlo and molecular dynamics trajectories. *J. Chem. Inf. Model.* **51**, 2007–2023 (2011).
68. Ramezani, F., Amanlou, M. & Rafii-Tabar, H. Gold nanoparticle shape effects on human serum albumin corona interface: A molecular dynamic study. *J. Nanopart. Res.* **16**, 2512 (2014).
69. Sambasivam, A., Sangwai, A. V. & Sureshkumar, R. Self-assembly of nanoparticle-surfactant complexes with rodlike micelles: A molecular dynamics study. *Langmuir* **32**, 1214–1219 (2016).
70. Antusek, A., Urban, M. & Sadlej, A. J. Lone pair interactions with coinage metal atoms: Weak van der Waals complexes of the coinage metal atoms with water and ammonia. *J. Chem. Phys.* **119**, 7247–7262 (2003).

Acknowledgements

The authors acknowledge the UNESCO UNISA Ithemba-LABS/NRF Africa Chair in Nanoscience & Nanotechnology (U2ACN2), the Centre for High-Performance Computing (CHPC), South Africa, and High-Performance Computing Centre (HPCC) of Sharif University of Technology, Iran, for providing computational resources and facilities for this research project. Z. J. acknowledges the developer group of Software for Chemistry & Materials (SCM) and computing resources of VU University of Amsterdam. The authors acknowledge Dr. D. Hamidi, who inspired us to investigate hydroxychloroquine. The authors dedicate this study to healthcare workers for their sacrifices in the pandemic.

Author contributions

P.R., M.A., and A.K. performed the MD simulations and analyzed the results, R. M. performed the QM calculations and analyzed the results, M.M. conceived the original idea and provided advice. Z. J. supervised the project, analyzed the results, and wrote the manuscript. All authors read and edited the manuscript.

Competing interests

The authors declare no competing interests.

Additional information

Supplementary Information The online version contains supplementary material available at <https://doi.org/10.1038/s41598-021-81617-6>.

Correspondence and requests for materials should be addressed to M.M. or Z.J.

Reprints and permissions information is available at www.nature.com/reprints.

Publisher's note Springer Nature remains neutral with regard to jurisdictional claims in published maps and institutional affiliations.



Open Access This article is licensed under a Creative Commons Attribution 4.0 International License, which permits use, sharing, adaptation, distribution and reproduction in any medium or format, as long as you give appropriate credit to the original author(s) and the source, provide a link to the Creative Commons licence, and indicate if changes were made. The images or other third party material in this article are included in the article's Creative Commons licence, unless indicated otherwise in a credit line to the material. If material is not included in the article's Creative Commons licence and your intended use is not permitted by statutory regulation or exceeds the permitted use, you will need to obtain permission directly from the copyright holder. To view a copy of this licence, visit <http://creativecommons.org/licenses/by/4.0/>.

© The Author(s) 2021